HHS Public Access

Author manuscript

Chem Eng J. Author manuscript; available in PMC 2021 September 15.

Published in final edited form as:

Chem Eng J. 2020 September 15; 396: . doi:10.1016/j.cej.2020.125239.

Immunologically modified $MnFe_2O_4$ nanoparticles to synergize photothermal therapy and immunotherapy for cancer treatment

Benqing Zhou[a,b,1], **Qiang Wu**[a,1], **Meng Wang**[a], **Ashley Hoover**[c], **Xin Wang**[a], **Feifan Zhou**[a], **Rheal A. Towner**[d], **Nataliya Smith**[d], **Debra Saunders**[d], **Jun Song**[a,*], **Junle Qu**[a,*], **Wei R. Chen**[c,*]

[a]Key Laboratory of Optoelectronic Devices and Systems of Ministry of Education and Guangdong Province, College of Physics and Optoelectronic Engineering, Shenzhen University, Shenzhen, 518060, P. R. China

[b]Department of Biomedical Engineering, College of Engineering, Shantou University, Shantou, 515063, P. R. China

[c]Biophotonics Research Laboratory, Center of Interdisciplinary Biomedical Education and Research, College of Mathematics and Science, University of Central Oklahoma, Edmond, Oklahoma, 73034, USA

[d]Advanced Magnetic Resonance Center, Oklahoma Medical Research Foundation, Oklahoma City, Oklahoma, 73104, USA

Abstract

Immunotherapy has been a promising candidate for cancer treatment. The combination of photothermal therapy (PTT) and immunotherapy have shown to cause tumor ablation and induce host immune response. However, this strategy is often hampered by a limited immune response and undesirable immunosuppression. In this work, we developed an immunologically modified nanoplatform, using ovalbumin (OVA)-coated PEGylated $MnFe_2O_4$ nanoparticles (NPs) loaded with R837 immunoadjuvant (R837-OVA-PEG-$MnFe_2O_4$ NPs) to synergize PTT and immunotherapy for the treatment of breast cancer. The designed R837-OVA-PEG-$MnFe_2O_4$ NPs are able to elicit significant immune responses *in vitro* and *in vivo*. $MnFe_2O_4$ NPs also allowed for a reduction of systemic immunosuppression through downregulation of M2-associated cytokines. More importantly, the R837-OVA-PEG-$MnFe_2O_4$ NPs under laser irradiation effectively inhibited tumor growth and prevented lung metastases, leading to a prolonged survival time and improved survival rate. In addition, the designed multitasking $MnFe_2O_4$ NPs showed as a good contrast agent for magnetic resonance (MR) imaging to detect orthotopic breast tumor *in vivo*. Our work provides a novel strategy for combined PTT and improved immunotherapy in the treatment of breast and other metastatic cancers.

*Corresponding author. songjun@szu.edu.cn (J. Song), jlqu@szu.edu.cn (J. Qu), and wchen@uco.edu (W. Chen).

[1]Authors contributed equally to this work.

Graphical Abstract

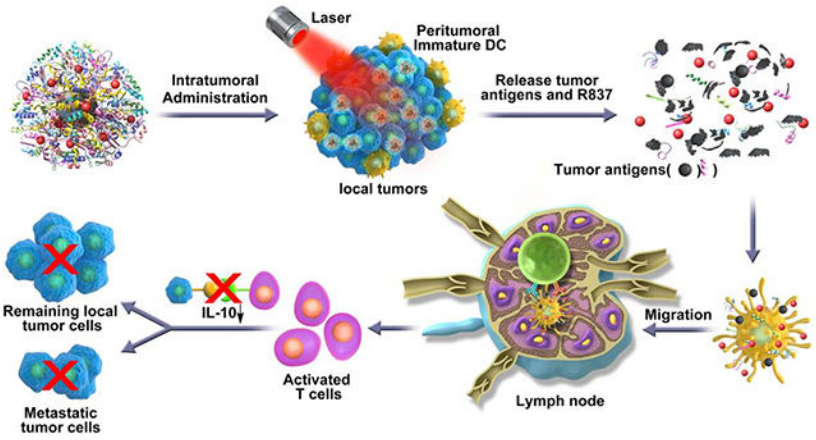

Keywords

$MnFe_2O_4$ nanoparticles; photothermal therapy; immunotherapy; immunoadjuvant; OVA

1. Introduction

Cancer immunotherapy has revolutionized the therapeutic landscape for patients with advanced cancers in recent years. It is worth noting that the 2018 Noble prize in physiology or medicine was awarded to James P. Allison and Tasuku Honjo for their discovery of cancer immunotherapy by inhibition of negative immune regulators [1–3]. To date, cancer immunotherapeutic strategies have included checkpoint blockade therapy (e.g., anti-programmed death-1/programmed death ligand (anti-PD-1/PD-L1) [4–7] and anti-cytotoxic T-lymphocyte-associated protein 4 (anti-CTLA-4) [8, 9]), adoptive T-cell transfer therapy [10, 11], as well as vaccine therapy [12–15], which have shown exciting clinical results. Nonetheless, the use of these immunotherapies alone are still demonstrated low efficacy in treating advanced cancers. A good cancer therapeutic strategy may include ablation of local tumors and induction of host immune response to kill the remaining tumor cells and prevent tumor recurrence [16]. Therefore, combining immunotherapy with other therapies, such as photodynamic therapy, chemotherapy, radiotherapy, and photothermal therapy (PTT), should significantly improve the clinical outcomes of cancer treatment [17–23].

With the rapid development of nanotechnology, various nanoparticles (NPs) have emerged as a powerful tool to combine cancer immunotherapy with other therapies [24–29]. For example, core-shell nanoscale coordination polymer NPs loaded with oxaliplatin and photosensitizer pyrolipid for chemotherapy/photodynamic therapy in combination with anti-PD-L1 checkpoint blockade could effectively inhibit primary tumors and contralaterally distant tumors [30]. Nanoscale metal-organic framework-based X-ray radiotherapy/radiodynamic therapy and immunotherapy has shown to significantly destroy local and distant tumors [31]. Near-infrared (NIR) light-induced PTT and immunotherapy *via* an antigen-capturing upconversion NPs (UCNPs) were designed for treatment of metastatic breast cancer [32]. The antigen-capturing UCNP-based combined PTT and immunotherapy

strategy could effectively destroy primary tumors in response to NIR laser irradiation and elicit significant antimetastatic effects by stimulating systemic antitumor immunity. Synergistic combination of local PTT and immunotherapy using glycated chitosan, a novel immunostimulant, was able to effectively treat advanced pancreatic cancer [33]. However, these strategies are often faced with low level of immune response rates or limited by immunosuppression.

Studies have proved that ovalbumin (OVA) is a strong immunogenic antigen and has been used as a proof of principle for numerous vaccination strategies [34–37]. Manganese ferrite ($MnFe_2O_4$) NPs are made up of iron oxide and manganese oxide NPs, in which iron oxide at a certain concentration could downregulate M2-associated cytokines, e.g., interleukin 10 (IL-10), induced immunosuppression in the body [38–40]. In addition, $MnFe_2O_4$ NPs display a favorable photothermal conversion property [41, 42], as well as magnetic resonance (MR) imaging property [43–45]. R837 immunoadjuvant as a Toll-like receptor-7 agonist is able to significantly stimulate the maturation of DC cells. However, R837 also cause a certain host immunosuppression, simultaneously [17, 26, 46]. In this study, we hypothesize that combined OVA protein and R837 adjuvant could stimulate DC cells more efficiently than nanovaccine or adjuvant alone. We use OVA protein modified PEGylated $MnFe_2O_4$ NPs loaded with R837 immunoadjuvant (R837-OVA-PEG-$MnFe_2O_4$ NPs) to synergize PTT and improved immunotherapy for treatment of orthotopic breast cancer. We found that the designed R837-OVA-PEG-$MnFe_2O_4$ NPs showed desirable cytocompatibility and photothermal stability, which could directly destroy local tumors through NIR-based PTT. They also elicited strong immune responses and reduced immunosuppression *in vitro* and *in vivo*. Most importantly, administration of R837-OVA-PEG-$MnFe_2O_4$ NPs in combination with laser irradiation significantly inhibited tumor growth and lung metastases. Besides, the multitasking $MnFe_2O_4$ NPs were as a desirable contrast agent for MR imaging to allow for precise detection of tumor.

2. Materials and methods

2.1. Materials

Manganese (II) acetylacetonate ($Mn(acac)_2$), iron (III) acetylacetonate ($Fe(acac)_3$), 1-octadecene (ODE, 90%), oleic acid (OA, 90%), oleylamine (OLA, 70%), benzyl ether, 1-octadecanol (99%), ovalbumin (OVA), and imiquimod (R837) were purchased from Sigma-Aldrich (St. Louis, MO). 1,2-hexadecanediol (98%) was obtained from TCI (Tokyo, Japan). 1,2-distearoyl-sn-glycero-3-phosphoethanolamine (DSPE) conjugated polyethylene glycol (DSPE-PEG, MW = 2000) was purchased from Ponsure Biotechnology (Shanghai, China). Dulbecco's Modified Eagle Medium (DMEM), RPMI-1640 medium, fetal bovine serum (FBS), 0.25% Trypsin-EDTA, penicillin, and streptomycin were purchased from Gibco (Grand Island, NY). Cell Counting Kit-8 (CCK-8) and double stain apoptosis detection kit (PI/calcein-AM) were purchased from Beyotime Biotechnology (Haimen, China). The Alexa Fluor 647-phalloidin was acquired from Cell Signaling Technology (Danvers, MA).

2.2. Synthesis of $MnFe_2O_4$ NPs

$MnFe_2O_4$ NPs were synthesized using a seed-mediated growth method [41, 47], In brief, $Mn(acac)_2$ (101.3 mg, 0.4 mmol), 1,2-hexadecanediol (1033.8 mg, 4 mmol), OA (2 mL), and OLA (2 mL) were mixed together using benzyl ether (24 mL) in a three-neck flask with mechanical stirring at 25 °C for 30 min in a vacuum. The mixture was then heated to 140 °C, and $Fe(acac)_3$ (282.5 mg, 0.8 mmol, 8 mL of benzyl ether) was added dropwise. Next, the mixture was heated to 260 °C for 30 min and cooled naturally to room temperature to produce $MnFe_2O_4$ seeds. Finally, the seeds would grow to $MnFe_2O_4$ NPs in a solution of $Fe(acac)_3$ and $Mn(acac)_2$ precursors. Briefly, $MnFe_2O_4$ seeds (0.2 mmol in 5 mL hexane) was mixed with $Mn(acac)_2$ (126.6 mg, 0.5 mmol), $Fe(acac)_3$ (353.1 mg, 1 mmol), 1-octadecanol (1352.5 mg, 5 mmol), OA (5 mL), OLA (5 mL), and benzyl ether (16 mL). The mixture was slowly heated up to 260 °C at an argon atmosphere for 30 min. The mixture was then cooled to room temperature to form $MnFe_2O_4$ NPs.

2.3. Synthesis of R837-OVA-PEG-$MnFe_2O_4$ NPs

The prepared $MnFe_2O_4$ NPs hexane solution (60 mg/mL, 1 mL) was added to 2 mL alcohol. The mixture was then centrifuged (12000 rpm, 15 min) to pellet $MnFe_2O_4$ NPs. The $MnFe_2O_4$ NPs pellet was dissolved in 5 mL CH_2Cl_2 and mixed with DSPE-PEG (20 mg/mL, 6 mL CH_2Cl_2) using ultrasonication for 20 min. The PEGylated $MnFe_2O_4$ NPs (PEG-$MnFe_2O_4$ NPs) were acquired *via* evaporation and washed with deionized water. The above PEG-$MnFe_2O_4$ NPs solution was then mixed with OVA (10 mg/mL, 6 mL water), and stirred for 12 h to form OVA-PEG-$MnFe_2O_4$ NPs. Lastly, R837 (0.4 mg/mL, 3 mL methanol) was added to OVA-PEG-$MnFe_2O_4$ NPs water solution (15 mL) under open stirring overnight to produce the final product of R837-OVA-PEG-$MnFe_2O_4$ NPs.

2.4. In vitro stimulation of DC cells

DC2.4 cells (5×10^5 per well) were seeded into a 12-well plate with 1 mL complete DMEM medium. After overnight incubation, these cells were treated with fresh DMEM medium (no FBS) containing PBS, PEG-$MnFe_2O_4$ NPs ([$MnFe_2O_4$] = 110 μg/mL), OVA-PEG-$MnFe_2O_4$ NPs ([$MnFe_2O_4$] = 110 μg/mL), R837-OVA-PEG-$MnFe_2O_4$ NPs ([$MnFe_2O_4$] = 110 μg/mL, [R837] = 2 μg/mL), or free R837 ([R837] = 2 μg/mL) for 24 h. The cell supernatants were then centrifuged (3000 rmp, 5 min), and DC activated cytokines in the supernatants including TNF-α, IL-6, and IL-10 were measured using quantikine enzyme-linked immunosorbent assay (ELISA) kits (Bio-Techne Ltd., R&D Systems, Minneapolis, MN) following the manufacturer's instructions. In addition, bone-marrow-derived dendritic cells (BMDCs) were treated with PBS, PEG-$MnFe_2O_4$ NPs ([$MnFe_2O_4$] = 55 μg/mL), OVA-PEG-$MnFe_2O_4$ NPs ([$MnFe_2O_4$] = 55 μg/mL), or R837-OVA-PEG-$MnFe_2O_4$ NPs ([$MnFe_2O_4$] = 55 μg/mL, [R837] = 1 μg/mL) for 24 h. These treated BMDCs were then stained with anti-mouse CD86-Brilliant Violet 605 (Biolegend, San Diego, CA), anti-mouse CD40-PE-Cy7 (Biolegend, San Diego, CA), and anti-mouse MHC-II-Alexa Fluor 700 (major histocompatibility complex class II, Thermo Fisher, Waltham, MA) antibodies before measurement by flow cytometry (Becton Dickinson FACSCalibur; New York, NY).

2.5. In vivo immune response

All animal procedures were performed in accordance with the Guidelines for Care and Use of Laboratory Animals published by the US National Institutes of Health (NIH) and approved by the University of Oklahoma Health Sciences Center (OUHSC) and Oklahoma Medical Research Foundation (OMRF) Institutional Animal Care and Use Committees (IACUC). BALB/C female mice (6–8 weeks) were purchased from Charles River (Wilmington, MA). 4T1 cells (5×10^4 per mouse) were subcutaneously injected into the right flank. Once tumor size reached about 100 mm^3, PEG-$MnFe_2O_4$ NPs, OVA-PEG-$MnFe_2O_4$ NPs, or R837-OVA-PEG-$MnFe_2O_4$ NPs PBS solution were injected into tumors at a $MnFe_2O_4$ dose of 1.0 mg per mouse, PBS (100 μL) as a control. These mice were then irradiated by an 805 nm laser for 10 min (1.2 W/cm^2) after 1 h intratumoral injection. Lymph nodes and blood were harvested on day 3 after these treatments. Tumors were also harvested on days 1 and 7 after these treatments. The spleens were harvested on day 7 after these treatments. Tumors were fixed, embedded in paraffin, sectioned, and immunostained with anti-mouse CD11c-Alexa Fluor 647 antibody on day 1 after treatment, or anti-mouse CD8-Alexa Fluor 647 antibody (Biolegend, San Diego, CA) on day 7 after treatment. Lymphocytes were treated and stained with anti-mouse CD11c-Alexa Fluor 647 and anti-mouse CD86-PE antibodies before flow cytometry analysis of DC maturation according to the manufacturer's instructions [26]. Splenocytes were treated and stained with anti-mouse CD3-APC/Cy7, anti-mouse CD4-PE, anti-mouse CD8-Alexa Flour 647, and anti-mouse IFN-γ-Alexa Flour 488 antibodies (Biolegend, San Diego, CA) before using flow cytometry analysis according to the manufacturer's instructions [48]. In addition, the number of 4T1 lung metastases was further investigated. In brief, the mice 15 days after treatment were injected with India ink through the trachea to obtain their lungs. Tumor metastasis areas appeared at white nodules on the surface of black lungs and were carefully counted.

2.6. In vivo antitumor efficacy

In vivo tumor therapy was evaluated by monitoring tumor volumes and survival rates. To establish orthotopic 4T1 breast tumors, 4T1 cells (5×10^4 per mouse) suspended in 100 μL RPMI-1640 medium were inoculated into the left breast fat pad. When tumor volumes were about 60 mm^3, these mice were randomly divided into 5 groups ($n = 6$ for each group) and treated with PBS plus laser irradiation (100 μL), PEG-$MnFe_2O_4$ NPs plus laser irradiation ([$MnFe_2O_4$] = 10 mg/mL, 100 μL), OVA-PEG-$MnFe_2O_4$ NPs plus laser irradiation ([$MnFe_2O_4$] = 10 mg/mL, 100 μL), R837-OVA-PEG-$MnFe_2O_4$ NPs plus laser irradiation ([$MnFe_2O_4$] = 10 mg/mL, 100 μL), or R837-OVA-PEG-$MnFe_2O_4$ NPs (no laser, [$MnFe_2O_4$] = 10 mg/mL, 100 μL). The power density and irradiation time were 1.2 W/cm^2 and 10 min, respectively. The tumor volumes were recorded until mice in the PBS plus laser irradiation group were moribund, or the tumor length was up to 20 mm. The survival rate was carefully monitored for 100 days post tumor inoculation.

2.7. Tumor MR imaging and in vivo biodistribution

Mice bearing orthotopic 4T1 breast tumors were first anesthetized using 1.5% isoflurane at 0.7 L/min oxygen and placed in a MR probe in a supine position before imaging using a Bruker Biospec 7 T horizontal-bore imaging spectrometer (Bruker BioSpin MRI GmbH,

Ettlingen, Germany). T_2 weighted MR images were generated by a Bruker S116 gradient coil (2.0 mT/m/A), a 72 mm quadrature multirung radiofrequency coil for radiofrequency transmission and signal reception. For orthotopic 4T1 breast tumor imaging, multiple MR imaging slices were put in the transverse plane through a spin-echo multislice (repetition time, 0.8 s; echo time (TE), 63 ms; 256 ×256 pixels matrix; 4 steps per acquisition; FOV, 3.5 × 3.5 cm^2; and slice thickness, 1mm) [49–51].

BALB/C female mice (6–8 weeks) were injected intravenously with PEGylated $MnFe_2O_4$ NPs ([$MnFe_2O_4$] = 10 mg/mL, [Fe] = 4.315 mg/mL, 100 μL in PBS for each mouse). Then these mice were sacrificed at different time points postinjection, and their major organs including tumor were harvested and weighed. Digestion of these organs by aqua regia for more than 12 h before using NexIon 300X inductively coupled plasma-mass spectrometry (ICP-MS, PerkinElmer, Waltham, MA) analysis of the Fe uptake in different organs.

3. Results and discussion

3.1. Formulation and characterization of R837-OVA-PEG-$MnFe_2O_4$ NPs

To synthesize R837-OVA-PEG-$MnFe_2O_4$ NPs, we first synthesized $MnFe_2O_4$ core particles, followed by coating with OVA protein and loading with R837 immunoadjuvant (Scheme 1).

Various techniques were used to characterize the particles. The monodispersed $MnFe_2O_4$ NPs with a diameter of 9.3 ± 1.1 nm were clearly observed (Fig. 1a). To determine the composition of the samples, elemental mapping analysis was performed. The particles were mainly comprised of Mn and Fe elements (Fig. S1). The UV-Vis spectrum of OVA-PEG-$MnFe_2O_4$ NPs and R837-OVA-PEG-$MnFe_2O_4$ NPs showed that $MnFe_2O_4$ NPs displayed a full-spectrum absorption from 200 to 900 nm (Fig. 1b), demonstrating that $MnFe_2O_4$ NPs could be used as a photothermal agent in a given NIR region. After loading with R837, new characteristic peaks of R837 at 310–330 nm appeared, indicating the successful loading of R837 (Fig. 1b). As shown in Fig. S2, the absorption values at 805 nm are positively correlated with their concentration, and R^2 is up to 0.9982. For example, when the concentration of $MnFe_2O_4$ NPs is 0.5 mg/mL, the absorptance at 805 nm reached 1.01 (Fig. S2). In addition, the loading efficiency of R837 (initially added R837/loaded R837) was 76.3% in accordance with the standard calibration curve of R837 (Fig. S3). The modification of DSPE-PEG and OVA protein was further confirmed by fourier-transform infrared spectroscopy (FTIR) spectra and thermogravimetric analysis (TGA). For OA-capped $MnFe_2O_4$ NPs, the C-H stretching vibration are located at 2920 and 2851 cm^{-1}, and the strong peaks at 1550 and 1427 cm^{-1} were related to the asymmetric and symmetric COO- stretching vibration of OA molecules (Fig. 1c). After the ligand exchange procedure, in the FTIR spectra of PEG-$MnFe_2O_4$ NPs, two new bands at 1732 and 1107 cm^{-1} appeared, corresponding to the stretching vibration of C=O and C-O of the PEG chains, respectively (Fig. 1c). In addition, the content of OVA (weight ratio of OVA/OVA-PEG-$MnFe_2O_4$ NPs) on the surface of NPs measured by TGA was 8.4% (Fig. 1d). As shown in Fig. 1e, after negative OVA protein coating, the zeta potential of PEG-$MnFe_2O_4$ NPs (−3.99 ± 1.52 mV) decreased to −15.37 ± 0.33 mV, indicating that OVA could further coat on the surface of the particles. After loading positively charged R837, the zeta potential of OVA-PEG-$MnFe_2O_4$ NPs increased to −12.60 ± 0.95 mV (Fig. 1e). This result further confirmed R837 was

successfully loaded on the particle surface through electrostatic adsorption. We then evaluated the photothermal effect of the R837-OVA-PEG-$MnFe_2O_4$ NPs. The formed R837-OVA-PEG-$MnFe_2O_4$ NPs at different concentrations under laser irradiation for 10 min could rapidly transform NIR light into thermal energy (Fig. 1f). For example, the temperature of the particles at the concentration of 2 mg/mL came up to 69 °C after laser irradiation for 10 min, whereas the temperature of water only reached 29 °C under the same conditions (Fig. 1f). Furthermore, the formed particles showed an excellent photothermal stability after five laser on/off cycles (Fig. S4). Therefore, these desirable photothermal properties served as quality control metrics to ensure PTT *in vitro* and *in vivo.*

3.2. Cytotoxicity assay

We used CCK-8 assay and morphological observation to evaluate the cytotoxicity of OVA-PEG-$MnFe_2O_4$ NPs. It was clear that the viability of 4T1 cells treated with OVA-PEG-$MnFe_2O_4$ at different concentrations ([$MnFe_2O_4$] = 0–400 μg/mL) was at least 90%, suggesting that the particles were noncytotoxic at the given concentration range (Fig. 2a). This result was further verified by morphology changes of the cells treated with the NPs. We found that the morphology of the cells treated by the NPs was well maintained and similar to PBS treated cells (Fig. S5). The cytoskeleton and the nucleus of the cells were also studied after being treated with OVA-PEG-$MnFe_2O_4$ NPs at the $MnFe_2O_4$ concentration of 200 μg/mL (Fig. S6). The cytoskeleton and nucleus of the cells treated with particles maintained well, similar to PBS control. Taken together, we can conclude that OVA-PEG-$MnFe_2O_4$ NPs show a favorable cytocompatibility in the given concentration range. It should be noted that R837 as a drug at a high concentration displays a certain cytotoxicity. However, in this work, R837 was loaded onto the surface of the particles with a very low concentration. Therefore, we used OVA-PEG-$MnFe_2O_4$ NPs instead of R837-OVA-PEG-$MnFe_2O_4$ NPs to evaluate their cytotoxicity. In addition, we also evaluated the cytotoxicity of R837-OVA-PEG-$MnFe_2O_4$ NPs. As shown in Fig. S7, we found that R837-OVA-PEG-$MnFe_2O_4$ NPs displayed no significant cytotoxicity. At the concentration of $MnFe_2O_4$ NPs below 200 μg/mL, the cell viability was more than 90%. Although at the concentration of 400 μg/mL, the cell viability was still up to 78.2%. The cytoskeleton staining further confirmed that the designed R837-OVA-PEG-$MnFe_2O_4$ NPs displayed no significant cytotoxicity at the $MnFe_2O_4$ NPs concentration of 200 μg/mL (Fig. S6).

In vitro PTT of OVA-PEG-$MnFe_2O_4$ NPs was further evaluated. As shown in Fig. 2b, under laser irradiation, the absolute cell viability decreased with increasing concentrations of the particles. For example, the viability of the cells treated with OVA-PEG-$MnFe_2O_4$ NPs ([$MnFe_2O_4$] = 400 μg/mL) plus laser irradiation decreased to 18.0 ± 4.2%, whereas the viability of the cells treated with PBS plus laser irradiation was 79.0 ± 1.4%. These results were further confirmed by live/dead dual-staining of the treated cells (Fig. 2c). We found that most of the cells were dead, indicated by red fluorescence, after being treated with OVA-PEG-$MnFe_2O_4$ NPs ([$MnFe_2O_4$] = 400 μg/mL) plus laser irradiation. Whereas, the cells treated with PBS or PBS plus laser irradiation were still viable, indicated by green fluorescence.

3.3. In vitro immune response

Dendritic cells (DCs) are as a kind of antigen-presenting cells (APCs) of the mammalian immune system. We used ELISA to assess the expression of cytokines secreted by DCs, including tumor necrosis factor-α (TNF-α), interleukin-6 (IL-6), and IL-10. As shown in Fig. 3a, the secretion levels of TNF-α from DCs after treatment with OVA-PEG-$MnFe_2O_4$ NPs, R837-OVA-PEG-$MnFe_2O_4$ NPs, or free R837 were all significantly increased, particularly for R837-OVA-PEG-$MnFe_2O_4$ NPs (652.0 ± 48.0 pg/mL) and free R837 (644.3 ± 52.0 pg/mL). In contrast, no obvious enhancement in TNF-α levels was observed after DCs were treated with PBS (60.8 ± 5.8 pg/mL) or PEG-$MnFe_2O_4$ NPs (83.0 ± 12.5 pg/mL). Similarly, the levels of IL-6 in Fig. 3b were significantly enhanced by R837-OVA-PEG-$MnFe_2O_4$ NPs (717.8 ± 21.6 pg/mL) and free R837 (434.7 ± 18.8 pg/mL). To assess the role of OVA protein in the nanoplatform, we used OVA protein alone to coculture with BMDCs. As shown in Fig. S8, S9, OVA protein alone also was able to effectively increase TNF-α and IL-6 cytokine secretion (Fig. S8) and maturate DC cells (Fig. S9). These results indicated that OVA protein and R837 immunoadjuvant both significantly increased the expression of M1-associated cytokines (e.g., TNF-α and IL-6). Meanwhile, R837 increased IL-10 expression, but, to a certain extent, $MnFe_2O_4$ moderately reduced IL-10 expression (Fig. 3c). Therefore, $MnFe_2O_4$ could downregulate the expression of M2-associated cytokines (e.g., IL-10), which decreases R837-induced immunosuppression. The reason may be that $MnFe_2O_4$ NPs are made up of iron oxide and manganese oxide NPs, in which iron oxide NPs could downregulate M2-associated cytokines (e.g., IL-10) induced immunosuppression in the body [38–40].

We then used flow cytometry to evaluate the percentages of mature DCs (e.g., $CD11c^+CD40^+$ and $CD11c^+CD86^+$) after cultivation with PBS, PEG-$MnFe_2O_4$ NPs, OVA-PEG-$MnFe_2O_4$ NPs, or R837-OVA-PEG-$MnFe_2O_4$ NPs (Fig. 4). The percentages of $CD11c^+CD40^+$ and $CD11c^+CD86^+$ cells in BMDCs after treatment with R837-OVA-PEG-$MnFe_2O_4$ NPs (70.8 ± 0.2% of $CD11c^+CD40^+$, and 43.2 ± 1.8% of $CD11c^+CD86^+$) was higher than that with OVA-PEG-$MnFe_2O_4$ NPs (49.7 ± 6.2% of $CD11c^+CD40^+$, and 30.4 ± 5.7% of $CD11c^+CD86^+$), PEG-$MnFe_2O_4$ NPs (38.9 ± 3.7% of $CD11c^+CD40^+$, and 23.9 ± 3.4% of $CD11c^+CD86^+$), and PBS (27.9 ± 2.5% of $CD11c^+CD40^+$, and 11.9 ± 0.9% of $CD11c^+CD86^+$). It is clear that OVA coating and R837 loading could significantly increase the maturation of DCs. MHC-II, a key component of antigen presentation to CD4 T cells, was also evaluated in BMDCs by flow cytometry. As shown in Fig. 4c, 4f, the expression level of MHC-II in BMDCs treated with R837-OVA-PEG-$MnFe_2O_4$ NPs (44.8 ± 1.2%) was higher than that of BMDCs treated with OVA-PEG-$MnFe_2O_4$ NPs (41.8 ± 4.5%), PEG-$MnFe_2O_4$ NPs (38.6 ± 3.5%), and PBS (20.1 ± 1.3%). Therefore, the designed R837-OVA-PEG-$MnFe_2O_4$ NPs induced a strong immune response *in vitro.*

To demonstrate the design of PTT induced immune response *in vitro*, we used a transwell system, where the 4T1 cells with different treatments and BMDCs were cultured in the upper and lower chamber separately, and the results are given in Fig. S10. As shown in Fig. S10, 4T1 cells treated with PTT could maturate and activate DC cells with the percentages of $CD11c^+CD80^+$ and $CD11c^+CD86^+$ mature DC cells up to 33.6 ± 0.2%, 32.6 ± 1.3%, respectively, whereas the 4T1 cells treated with BMDCs is only 6.5 ± 0.6% of CD11c

$^{+}CD80^{+}$ and 6.6 ± 0.2% of $CD11c^{+}CD86^{+}$. This may be due to PTT induced tumor specific antigen from 4T1 cells. It should be noted that digested cells using trypsin may also produce fragments from 4T1 tumor cells, which could also maturate DC cells. However, 4T1 cells treated with PTT were more efficient in activating DC cells than 4T1 tumor cells without PTT (*, p = 0.01087 of $CD11c^{+}CD80^{+}$; **, p = 0.00576 of $CD11c^{+}CD86^{+}$).

3.4. In vivo immune response

To research *in vivo* immune response induced by R837-OVA-PEG-$MnFe_2O_4$ NPs under laser irradiation, we first harvested blood from 4T1 tumor-bearing mice on day 3 after different treatments. Cytokines including TNF-α, IL-6, and IL-10 in serum were analyzed by ELISA. As shown in Fig. 5a, 5b, the levels of TNF-α and IL-6 on day 3 after treatment with R837-OVA-PEG-$MnFe_2O_4$ NPs plus laser irradiation were higher than those of other treatments. However, the levels of IL-10 in serum from mice treated with PEG-$MnFe_2O_4$ NPs plus laser irradiation or OVA-PEG-$MnFe_2O_4$ NPs plus laser irradiation were lower than those in mice treated with PBS plus laser irradiation or R837-OVA-PEG-$MnFe_2O_4$ plus laser irradiation (Fig. 5c). This result indicated that $MnFe_2O_4$ NPs were able to downregulate the expression of IL-10 *in vivo*, which was consistent with *in vitro* immune response data (Fig. 3c). Therefore, the designed $MnFe_2O_4$-based NPs have the potential to reduce R837-induced immunosuppression *in vitro* and *in vivo*.

Lymphocytes were isolated from the lymph nodes of mice on day 3 after PTT treatments, followed by flow cytometry analysis (Fig. 1). We observed that R837-OVA-PEG-$MnFe_2O_4$ NPs under irradiation with an 805 nm laser could produce a higher level of DC maturation ($CD11c^{+}CD86^{+}$) than other treatments. As shown in Fig. 1a, 1d, the percentage of mature DCs was highest in mice treated with R837-OVA-PEG-$MnFe_2O_4$ NPs plus laser irradiation (21.3 ± 0.1%). Decreasing amounts of mature DCs were detected in mice treated with OVA-PEG-$MnFe_2O_4$ NPs plus laser irradiation (19.3 ± 0.9%), PEG-$MnFe_2O_4$ NPs plus laser irradiation (18.4 ± 0.6%), and PBS plus laser irradiation (13.6 ± 0.3%).

Next, to address whether R837-OVA-PEG-$MnFe_2O_4$ NPs under laser irradiation could induce systemic T-cell activation, we evaluated the production of antitumor TNF-γ-secreting $CD3^{+}CD4^{+}$ and $CD3^{+}CD8^{+}$ T cells by splenocytes from mice on day 7 after different treatments. The gating strategies were analysed in Fig. S11. It was found that splenocytes from mice treated with R837-OVA-PEG-$MnFe_2O_4$ NPs plus laser irradiation showed a much higher percentage of TNF-γ-secreting $CD3^{+}CD4^{+}$ up to 1.16 ± 0.07% (Fig. 1b, 1e) and $CD3^{+}CD8^{+}$ T cells up to 1.13 ± 0.17% (Fig. 1c, 1f). These results demonstrated that R837-OVA-PEG-$MnFe_2O_4$ NPs based PTT, compared with OVA-PEG-$MnFe_2O_4$ NPs or PEG-$MnFe_2O_4$ NPs based PTT, were more effective in inducing immune response *in vivo*.

Finally, we used immunofluorescence to further confirm whether R837-OVA-PEG-$MnFe_2O_4$ NPs under laser irradiation could induce tumor infiltrating DC maturation and T cell activation. We found that DCs (red fluorescence) were obviously increased in tumor-bearing mice on day 1 after treatment with R837-OVA-PEG-$MnFe_2O_4$ NPs plus laser irradiation, in comparison with the PBS plus laser irradiation control (Fig. S12). As shown in Fig. S13, R837-OVA-PEG-$MnFe_2O_4$ NPs plus laser irradiation also effectively enhanced $CD8^{+}$ T-cell infiltration (green fluorescence). These results furthor demonstrated that R837-

OVA-PEG-$MnFe_2O_4$ NPs based PTT could induce strong *in vivo* response. In addition, Treg-$Foxp3^+$ related red fluorescence was increased higher by R837 loaded particles (R837-OVA-PEG-$MnFe_2O_4$ NPs) plus laser irradiation than OVA-PEG-$MnFe_2O_4$ NPs (without R837 loading) plus laser irradiation (Fig. S14). Therefore, to a certain extent, R837 adjuvant could cause immunosuppression *in vivo*. As mentioned above, R837 can function as both immune stimulator and immune suppressor. However, thanks to the positive effect of R837, in conjunction with OVA and laser irradiation, we utilized the immunostimulation effects of R837 to enhance the anti-tumor effect.

3.5. In vivo antitumor efficacy

We then assessed the antitumor efficacy of R837-OVA-PEG-$MnFe_2O_4$ NPs based PTT using an orthotopic 4T1 breast tumor model. As shown in Fig. 7a, under laser irradiation, these $MnFe_2O_4$-based NPs could significantly transfer NIR light into thermal energy *in vivo*. The temperatures of these $MnFe_2O_4$ NP-based PTT treated tumor regions were more than 50 °C after irradiation for 2 min, and kept around 55 °C during the laser treatment, whereas the temperature of the PBS plus laser irradiation was lower than 42 °C after irradiation for 10 min. Under laser irradiation, these $MnFe_2O_4$ NP-based PTT treated groups experienced significant tumor inhibition, especially for OVA-PEG-$MnFe_2O_4$ NPs+L and R837-OVA-PEG-$MnFe_2O_4$ NPs+L (complete tumor regression, Fig. 7b). Importantly, we found that the intratumoral injection of R837-OVA-PEG-$MnFe_2O_4$ NPs under laser irradiation could effectively increase the survival rates (Fig. 7c). Under the research time period (100 days), the mice treated with R837-OVA-PEG-$MnFe_2O_4$ NPs plus laser irradiation still had a survival rate of 33.3%, whereas, no mouse survived under other treatments (Fig. 7c). It should be noted that R837-OVA-PEG-$MnFe_2O_4$ NPs plus laser irradiation was more efficient in preventing lung metastases on day 15 after treatment (32.5 ± 8.5 of number of 4T1 lung metastases) than other treatments (***$p < 0.001$ vs. PBS plus laser irradiation, Fig. 7d). Therefore, under laser irradiation, R837-OVA-PEG-$MnFe_2O_4$ NPs have a great antitumor efficacy *in vivo* and inhibit metastatic tumor cells, largely due to following factors: (1) Tumor spectific antigens were produced by R837-OVA-PEG-$MnFe_2O_4$ NPs based PTT; (2) the antigens then processed and presented by APCs to elicit the proliferation of tumor-specific effector T cells in lymph nodes with the help of R837 adjuvant and OVA protein; (3) $MnFe_2O_4$ NPs downregulated R837-induced immunosuppression. These processes are vividly depicted in Scheme 1. While the detailed mechanism is still under investigation, we hypothesize the synergistic effect as follows. OVA protein stimulates a general host immune response and R837 stimulates a specific immune response when combined with released tumor antigens induced by PTT.

3.6. Tumor MR imaging and in vivo biodistribution

The immunologically modified nanoplateform in the current study not only served as an efficient delivery vehicle for PTT and immunotherapy, but also served as an effective T_2-weighted MR imaging contrast agent for detection of orthotopic breast cancer. As shown in Fig. 8a, the tumor region became dark after injection of the multitasking $MnFe_2O_4$ NPs, suggesting that the particles could be effectively delivered into the tumor region for precise detection of tumors using MR imaging. Additionally, when we enlarge tumor sites before injection and 3 h postinjection, T_2 MR signal reduce distinctly, especially at tumor edges

(Fig. 8b). Quantitative analysis of the MR signal/noise ratio (SNR) of tumor showed that the SNR of the tumor decreased from 2.1 (pre-injection) to 1.2 at 3 h postinjection, and then returned to 1.8 at 24 h postinjection (Fig. 8c), which was consistent with Fig. 8a.

In addition, we found that the particles were mainly taken up by the liver and spleen, and the particles could be metabolized stepwise 7 days postinjection, which was also verified by long-term histologic changes in the major organs (Fig. S15). We found that there is no histological change observed in the major organ slices one month after injection, compared with the PBS control (Fig. S16). These results indicated that the designed particles had a desirable biocompatibility *in vivo*.

4. Conclusions

We have developed photothermostable and biocompatible immunologically modified nanoplatform, R837-OVA-PEG-$MnFe_2O_4$, to combine PTT with immunotherapy for treatment of breast cancer. Owing to the synergy of R837 immunoadjuvant, OVA protein, and manganese iron oxide, the formed R837-OVA-PEG-$MnFe_2O_4$ NPs significantly induce DC maturation through enhanced M1-associated cytokine expression and reduced R837-induced M2-associated cytokine expression. Importantly, R837-OVA-PEG-$MnFe_2O_4$ NPs based PTT not only effectively produced $CD11c^+CD86^+$ mature DC cells and IFN-γ^+ T cells, but also reduced immunosuppression *in vivo*. In addition, this multitasking $MnFe_2O_4$ NPs were shown as a desirable contrast agent for MR imaging to allow for the precise diagnosis of tumors. We believe that combination of PTT and improved immunotherapy for the treatment of breast cancer using immunologically modified $MnFe_2O_4$ NPs holds a tremendous promise in the treatment of advanced cancers.

Supplementary Material

Refer to Web version on PubMed Central for supplementary material.

Acknowledgements

This research is supported by the National Natural Science Foundation of China (61805161, 61805158, 61775145, 61525503, 61620106016, 61835009, and 81727804), and Shenzhen Basic Research Project (JCYJ20170818143045740). This work also been partially supported by the U.S. National Institutes of Health (R01CA205348–01, RS20132225–106, and R21 EB 015509–01), and the Oklahoma Center for the Advancement of Science and Technology (HR16–085).

References

[1]. Chowdhury PS, Chamoto K, Kumar A, Honjo T, PPAR-Induced fatty acid oxidation in T cells increases the number of tumor-reactive CD8(+) T cells and facilitates anti-PD-1 therapy, Cancer Immunol. Res. 6 (2018) 1375–1387. [PubMed: 30143538]

[2]. Miyajima M, Zhang BH, Sugiura Y, Sonomura K, Guerrini MM, Tsutsui Y, Maruya M, Vogelzang A, Chamoto K, Honda K, Hikida T, Ito S, Qin HY, Sanuki R, Suzuki K, Furukawa T, Ishihama Y, Matsuda F, Suematsu M, Honjo T, Fagarasan S, Metabolic shift induced by systemic activation of T cells in PD-1-deficient mice perturbs brain monoamines and emotional behavior, Nat. Immunol. 18 (2017) 1342–1352. [PubMed: 29058703]

[3]. Wei SC, Duffy CR, Allison JP, Fundamental mechanisms of immune checkpoint blockade therapy, Cancer Discovery 8 (2018) 1069–1086. [PubMed: 30115704]

[4]. Kosmides AK, Meyer RA, Hickey JW, Aje K, Cheung KN, Green JJ, Schneck JP, Biomimetic biodegradable artificial antigen presenting with PD-1 blockade to treat melanoma cells synergize, Biomaterials 118 (2017) 16–26. [PubMed: 27940380]

[5]. Gubin MM, Zhang XL, Schuster H, Caron E, Ward JP, Noguchi T, Ivanova Y, Hundal J, Arthur CD, Krebber WJ, Mulder GE, Toebes M, Vesely MD, Lam SSK, Korman AJ, Allison JP, Freeman GJ, Sharpe AH, Pearce EL, Schumacher TN, Aebersold R, Rammensee HG, Melief CJM, Mardis ER, Gillanders WE, Artyomov MN, Schreiber RD, Checkpoint blockade cancer immunotherapy targets tumour-specific mutant antigens, Nature 515 (2014) 577–581. [PubMed: 25428507]

[6]. Pardoll DM, The blockade of immune checkpoints in cancer immunotherapy, Nat. Rev. Cancer 12 (2012) 252–264. [PubMed: 22437870]

[7]. Zou MZ, Liu WL, Li CX, Zheng DW, Zeng JY, Gao F, Ye JJ, Zhang XZ, A multifunctional biomimetic nanoplatform for relieving hypoxia to enhance chemotherapy and inhibit the PD-1/PD-L1 axis, Small 14 (2018) 1801120.

[8]. Ribas A, Wolchok JD, Cancer immunotherapy using checkpoint blockade, Science 359 (2018) 1350–1355. [PubMed: 29567705]

[9]. Ravi R, Noonan KA, Pham V, Bedi R, Zhavoronkov A, Ozerov IV, Makarev E, Artemov AV, Wysocki PT, Mehra R, Nimmagadda S, Marchionni L, Sidransky D, Borrello IM, Izumchenko E, Bedi A, Bifunctional immune checkpoint-targeted antibody-ligand traps that simultaneously disable TGF beta enhance the efficacy of cancer immunotherapy, Nat. Commun. 9 (2018) 741. [PubMed: 29467463]

[10]. Fry TJ, Shah NN, Orentas RJ, Stetler-Stevenson M, Yuan CM, Ramakrishna S, Wolters P, Martin S, Delbrook C, Yates B, Shalabi H, Fountaine TJ, Shern JF, Majzner RG, Stroncek DF, Sabatino M, Feng Y, Dimitrov DS, Zhang L, Nguyen S, Qin HY, Dropulic B, Lee DW, Mackall CL, CD22-targeted CAR T cells induce remission in B-ALL that is naive or resistant to CD19-targeted CAR immunotherapy, Nat. Med. 24 (2018) 20–28. [PubMed: 29155426]

[11]. June CH, O'Connor RS, Kawalekar OU, Ghassemi S, Milone MC, CAR T cell immunotherapy for human cancer, Science 359 (2018) 1361–1365. [PubMed: 29567707]

[12]. Duong HTT, Yin Y, Thambi T, Nguyen TL, Phan VHG, Lee MS, Lee JE, Kim J, Jeong JH, Lee DS, Smart vaccine delivery based on microneedle arrays decorated with ultra pH-responsive copolymers for cancer immunotherapy, Biomaterials 185 (2018) 13–24. [PubMed: 30216806]

[13]. Liu LN, Wang YH, Miao L, Liu Q, Musetti S, Li J, Huang L, Combination immunotherapy of MUC1 mRNA nano-vaccine and CTLA-4 blockade effectively inhibits growth of triple negative breast cancer, Mol. Ther. 26 (2018) 45–55. [PubMed: 29258739]

[14]. Marin-Acevedo JA, Soyano AE, Dholaria B, Knutson KL, Lou YY, Cancer immunotherapy beyond immune checkpoint inhibitors, J. Hematol. Oncol. 11 (2018) 8. [PubMed: 29329556]

[15]. Hansen SG, Ford JC, Lewis MS, Ventura AB, Hughes CM, Coyne-Johnson L, Whizin N, Oswald K, Shoemaker R, Swanson T, Legasse AW, Chiuchiolo MJ, Parks CL, Axthelm MK, Nelson JA, Jarvis MA, Piatak M, Lifson JD, Picker LJ, Profound early control of highly pathogenic SIV by an effector memory T-cell vaccine, Nature 473 (2011) 523–527. [PubMed: 21562493]

[16]. He YC, Cong C, He YQ, Hao ZN, Li CH, Wang S, Zhao QQ, He HY, Zhu RY, Li XL, Gao DW, Tumor hypoxia relief overcomes multidrug resistance and immune inhibition for self-enhanced photodynamic therapy, Chem. Eng. J. 375 (2019) 122079.

[17]. Xu J, Xu LG, Wang CY, Yang R, Zhuang Q, Han X, Dong ZL, Zhu WW, Peng R, Liu Z, Near-infrared-triggered photodynamic therapy with multitasking upconversion nanoparticles in combination with checkpoint blockade for immunotherapy of colorectal cancer, ACS Nano 11 (2017) 4463–4474. [PubMed: 28362496]

[18]. Zhou B, Song J, Wang M, Wang X, Wang J, Howard EW, Zhou F, Qu J, Chen WR, BSA-bioinspired gold nanorods loaded with immunoadjuvant for the treatment of melanoma by combined photothermal therapy and immunotherapy, Nanoscale 10 (2018) 21640–21647. [PubMed: 30232481]

[19]. Lu K, He C, Guo N, Chan C, Ni K, Weichselbaum RR, Lin W, Chlorin-based nanoscale metal-organic framework systemically rejects colorectal cancers via synergistic photodynamic therapy and checkpoint blockade immunotherapy, J. Am. Chem. Soc. 138 (2016) 12502–12510. [PubMed: 27575718]

[20]. Song Q, Yin Y, Shang L, Wu T, Zhang D, Kong M, Zhao Y, He Y, Tan S, Guo Y, Zhang Z, Tumor microenvironment responsive nanogel for the combinatorial antitumor effect of chemotherapy and immunotherapy, Nano Lett. 17 (2017) 6366–6375. [PubMed: 28858519]

[21]. Zhou FF, Wu S, Song S, Chen WR, Resasco DE, Xing D, Antitumor immunologically modified carbon nanotubes for photothermal therapy, Biomaterials 33 (2012) 3235–3242. [PubMed: 22296829]

[22]. Guo LR, Yan DD, Yang DF, Li YJ, Wang XD, Zalewski O, Yan BF, Lu W, Combinatorial photothermal and immuno cancer therapy using chitosan-coated hollow copper sulfide nanoparticles, ACS Nano 8 (2014) 5670–5681. [PubMed: 24801008]

[23]. Gao F, Zhang C, Qiu WX, Dong X, Zheng DW, Wu W, Zhang XZ, PD-1 blockade for improving the antitumor efficiency of polymer-doxorubicin nanoprodrug, Small 14 (2018) 1802403.

[24]. Burga RA, Patel S, Bollard CM, Cruz CRY, Fernandes R, Conjugating prussian blue nanoparticles onto antigen-specific t cells as a combined nanoimmunotherapy, Nanomedicine 11 (2016) 1759–1767. [PubMed: 27389189]

[25]. Yata T, Takahashi Y, Tan MM, Nakatsuji H, Ohtsuki S, Murakami T, Imahori H, Umeki Y, Shiomi T, Takakura Y, Nishikawa M, DNA nanotechnology-based composite-type gold nanoparticle-immunostimulatory DNA hydrogel for tumor photothermal immunotherapy, Biomaterials 146 (2017) 136–145. [PubMed: 28918263]

[26]. Chen Q, Xu LG, Liang C, Wang C, Peng R, Liu Z, Photothermal therapy with immune-adjuvant nanoparticles together with checkpoint blockade for effective cancer immunotherapy, Nat. Commun. 7 (2016) 13193. [PubMed: 27767031]

[27]. Duan XP, Chan C, Guo NN, Han WB, Weichselbaum RR, Lin WB, Photodynamic therapy mediated by nontoxic core-shell nanoparticles synergizes with immune checkpoint blockade to elicit antitumor immunity and antimetastatic effect on breast cancer, J. Am. Chem. Soc. 138 (2016) 16686–16695. [PubMed: 27976881]

[28]. Bauleth-Ramos T, Shahbazi MA, Liu D, Fontana F, Correia A, Figueiredo P, Zhang H, Martins JP, Hirvonen JT, Granja P, Nutlin-3a and cytokine co-loaded spermine-modified acetalated dextran nanoparticles for cancer chemo-immunotherapy, Adv. Funct. Mater. 27 (2017) 1703303.

[29]. Mottas I, Bekdemir A, Cereghetti A, Spagnuolo L, Yang YSS, Muller M, Irvine DJ, Stellacci F, Bourquin C, Amphiphilic nanoparticle delivery enhances the anticancer efficacy of a TLR7 ligand via local immune activation, Biomaterials 190 (2019) 111–120. [PubMed: 30415018]

[30]. He CB, Duan XP, Guo NN, Chan C, Poon C, Weichselbaum RR, Lin WB, Core-shell nanoscale coordination polymers combine chemotherapy and photodynamic therapy to potentiate checkpoint blockade cancer immunotherapy, Nat. Commun. 7 (2016) 12499. [PubMed: 27530650]

[31]. Lu KD, He CB, Guo NN, Chan C, Ni KY, Lan GX, Tang HD, Pelizzari C, Fu YX, Spiotto MT, Weichselbaum RR, Lin WB, Low-dose X-ray radiotherapy-radiodynamic therapy via nanoscale metal-organic frameworks enhances checkpoint blockade immunotherapy, Nat. Biomed. Eng 2 (2018) 600–610. [PubMed: 31015630]

[32]. Wang M, Song J, Zhou FF, Hoover AR, Murray C, Zhou BQ, Wang L, Qu JL, Chen WR, NIR-triggered phototherapy and immunotherapy via an antigen-capturing nanoplatform for metastatic cancer treatment, Adv. Sci. 6 (2019) 1802157.

[33]. Zhou F, Yang J, Zhang Y, Liu M, Lang ML, Li M, Chen WR, Local phototherapy synergizes with immunoadjuvant for treatment of pancreatic cancer through induced immunogenic tumor vaccine, Clin. Cancer Res. 24 (2018) 5335–5346. [PubMed: 30068705]

[34]. Assudani D, Cho HI, DeVito N, Bradley N, Celis E, In vivo expansion, persistence, and function of peptide vaccine-induced CD8 T cells occur independently of CD4 T cells, Cancer Res. 68 (2008) 9892–9899. [PubMed: 19047170]

[35]. Pan JB, Wang YQ, Zhang C, Wang XY, Wang HY, Wang JJ, Yuan YZ, Wang X, Zhang XJ, Yu CS, Sun SK, Yan XP, Antigen-directed fabrication of a multifunctional nanovaccine with ultrahigh antigen loading efficiency for tumor photothermal-immunotherapy, Adv. Mater. 30 (2018) 1704408.

[36]. Guan XW, Chen J, Hu YY, Lin L, Sun PJ, Tian H, Chen XS, Highly enhanced cancer immunotherapy by combining nanovaccine with hyaluronidase, Biomaterials 171 (2018) 198–206. [PubMed: 29698869]

[37]. Li S, Qu YC, Yu XF, Xue W, Liu ZH, Cell membrane adhesive n-hexadecyl choline phosphate as vaccine delivery systems for anticancer immunotherapy, Chem. Eng. J. 360 (2019) 402–414.

[38]. Zanganeh S, Hutter G, Spitler R, Lenkov O, Mahmoudi M, Shaw A, Pajarinen JS, Nejadnik H, Goodman S, Moseley M, Coussens LM, Daldrup-Link HE, Iron oxide nanoparticles inhibit tumour growth by inducing pro-inflammatory macrophage polarization in tumour tissues, Nat. Nanotechnol. 11 (2016) 986–994. [PubMed: 27668795]

[39]. Daldrup-Link HE, Golovko D, Ruffell B, DeNardo DG, Castaneda R, Ansari C, Rao JH, Tikhomirov GA, Wendland MF, Corot C, Coussens LM, MRI of tumor-associated macrophages with clinically applicable iron oxide nanoparticles, Clin. Cancer Res. 17 (2011) 5695–5704. [PubMed: 21791632]

[40]. Chiang CS, Lin YJ, Lee R, Lai YH, Cheng HW, Hsieh CH, Shyu WC, Chen SY, Combination of fucoidan-based magnetic nanoparticles and immunomodulators enhances tumour-localized immunotherapy, Nat. Nanotechnol. 13 (2018) 746–754. [PubMed: 29760523]

[41]. Wu Q, Lin Y, Wo F, Yuan Y, Ouyang Q, Song J, Qu J, Yong K-T, Novel magnetic-luminescent janus nanoparticles for cell labeling and tumor photothermal therapy, Small 13 (2017) 1701129.

[42]. Chen YY, Deng XR, Li CX, He F, Liu B, Hou ZY, Cheng ZY, Xing BG, Lin J, Stimuli-responsive nanocomposites for magnetic targeting synergistic multimodal therapy and T-1/T-2-weighted dual-mode imaging, Nanomed.-Nanotechnol. Biol. Med. 13 (2017) 875–883.

[43]. Ding B, Shao S, Xiao H, Sun C, Cai X, Jiang F, Zhao X, Ma P.a., Lin J, MnFe2O4-decorated large-pore mesoporous silica-coated upconversion nanoparticles for near-infrared light-induced and O2 self-sufficient photodynamic therapy, Nanoscale 11 (2019) 14654–14667. [PubMed: 31355836]

[44]. Yang H, Zhang CX, Shi XY, Hu H, Du XX, Fang Y, Ma YB, Wu HX, Yang SP, Water-soluble superparamagnetic manganese ferrite nanoparticles for magnetic resonance imaging, Biomaterials 31 (2010) 3667–3673. [PubMed: 20144480]

[45]. Sahoo B, Devi KSP, Dutta S, Maiti TK, Pramanik P, Dhara D, Biocompatible mesoporous silica-coated superparamagnetic manganese ferrite nanoparticles for targeted drug delivery and MR imaging applications, J. Colloid Interface Sci. 431 (2014) 31–41. [PubMed: 24980623]

[46]. Harwood CA, Perrett CM, Brown VL, Leigh IM, McGregor JM, Proby CM, Imiquimod cream 5% for recalcitrant cutaneous warts in immunosuppressed individuals, Br. J. Dermatol. 152 (2005) 122–129. [PubMed: 15656812]

[47]. Song Q, Zhang ZJ, Controlled synthesis and magnetic properties of bimagnetic spinel ferrite $CoFe_2O_4$ and $MnFe_2O_4$ nanocrystals with core-shell architecture, J. Am. Chem. Soc. 134 (2012) 10182–10190. [PubMed: 22621435]

[48]. Min YZ, Roche KC, Tian SM, Eblan MJ, McKinnon KP, Caster JM, Chai SJ, Herring LE, Zhang LZ, Zhang T, DeSimone JM, Tepper JE, Vincent BG, Serody JS, Wang AZ, Antigen-capturing nanoparticles improve the abscopal effect and cancer immunotherapy, Nat. Nanotechnol. 12 (2017) 877–882. [PubMed: 28650437]

[49]. Doblas S, He T, Saunders D, Pearson J, Hoyle J, Smith N, Lerner M, Towner RA, Glioma morphology and tumor-induced vascular alterations revealed in seven rodent glioma models by in vivo magnetic resonance imaging and angiography, J. Magn. Reson. Imaging 32 (2010) 267–275. [PubMed: 20677250]

[50]. Towner RA, Jensen RL, Colman H, Vaillant B, Smith N, Casteel R, Saunders D, Gillespie DL, Silasi-Mansat R, Lupu F, Giles CB, Wren JD, ELTD1, a potential new biomarker for gliomas, Neurosurgery 72 (2013) 77–90.

[51]. Ziegler J, Pody R, de Souza PC, Evans B, Saunders D, Smith N, Mallory S, Njoku C, Dong YZ, Chen H, Dong JL, Lerner M, Mian O, Tummala S, Battiste J, Fung KM, Wren JD, Towner RA, ELTD1, an effective anti-angiogenic target for gliomas: preclinical assessment in mouse GL261 and human G55 xenograft glioma models, Neuro-Oncology 19 (2017) 175–185. [PubMed: 27416955]

Highlights

- Immunologically modified $MnFe_2O_4$ NPs were constructed for combined PTT and immunotherapy.
- The $MnFe_2O_4$ NPs elicited strong immune responses *in vitro* and *in vivo*.
- The $MnFe_2O_4$ NPs based PTT effectively inhibited tumor growth and lung metastases.
- The feasible mechanism for combined PTT and immunotherapy was clearly described.
- The $MnFe_2O_4$ NPs showed as a desirable MR contrast agent for tumor imaging.

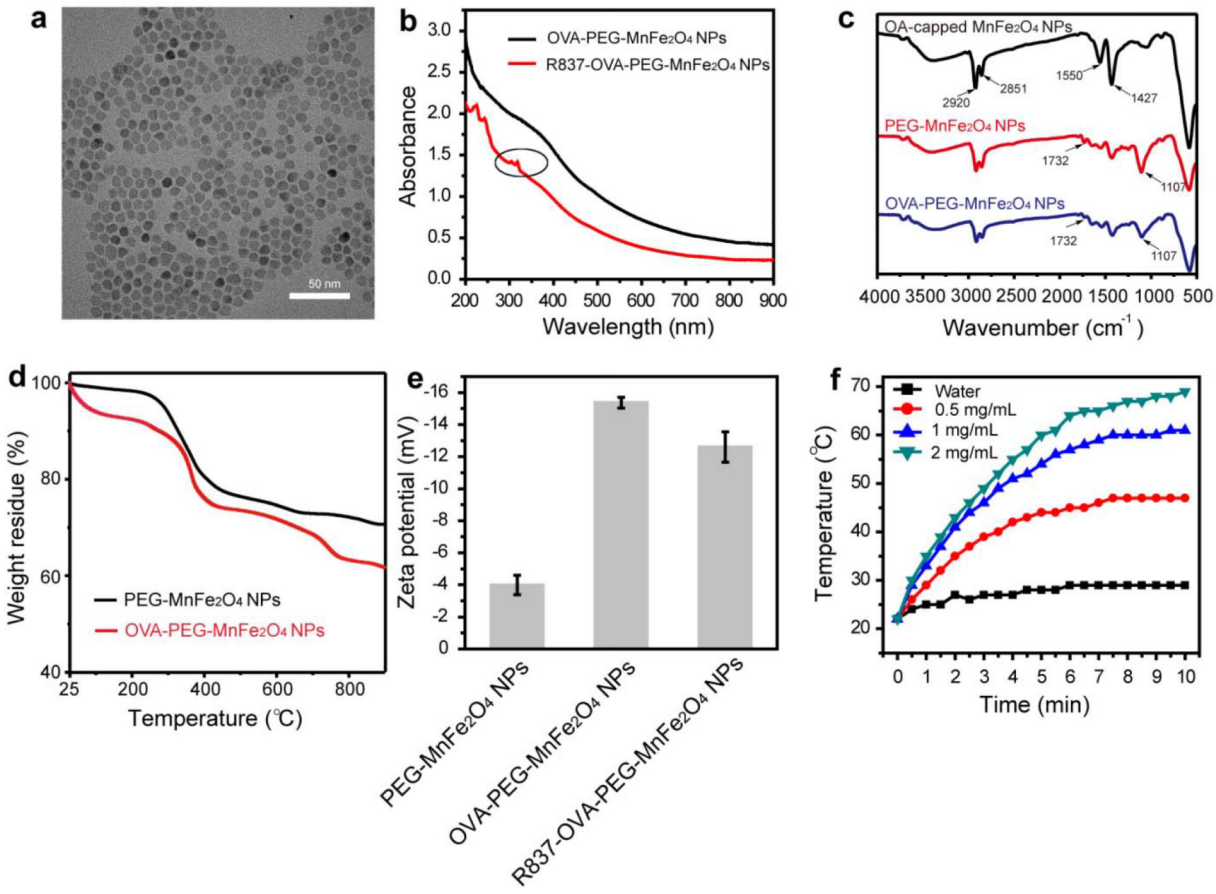

Fig. 1.

(a) Transmission electron microscopy (TEM) image of OA-capped $MnFe_2O_4$ NPs. (b) UV-vis spectrum of OVA-PEG-$MnFe_2O_4$ NPs and R837-OVA-PEG-$MnFe_2O_4$ NPs (the circle refers to R837 characteristic peaks). (c) FTIR spectrum of OA-capped $MnFe_2O_4$ NPs, PEG-$MnFe_2O_4$ NPs, and OVA-PEG-$MnFe_2O_4$ NPs, respectively. (d) TGA of PEG-$MnFe_2O_4$ NPs and OVA-PEG-$MnFe_2O_4$ NPs. (e) Zeta potential of PEG-$MnFe_2O_4$ NPs, OVA-PEG-$MnFe_2O_4$ NPs, and R837-OVA-PEG-$MnFe_2O_4$ NPs, respectively. (f) Temperature of water and R837-OVA-PEG-$MnFe_2O_4$ NPs dispersed in water at different concentrations under irradiation with an 805 nm laser (1.2 W/cm^2).

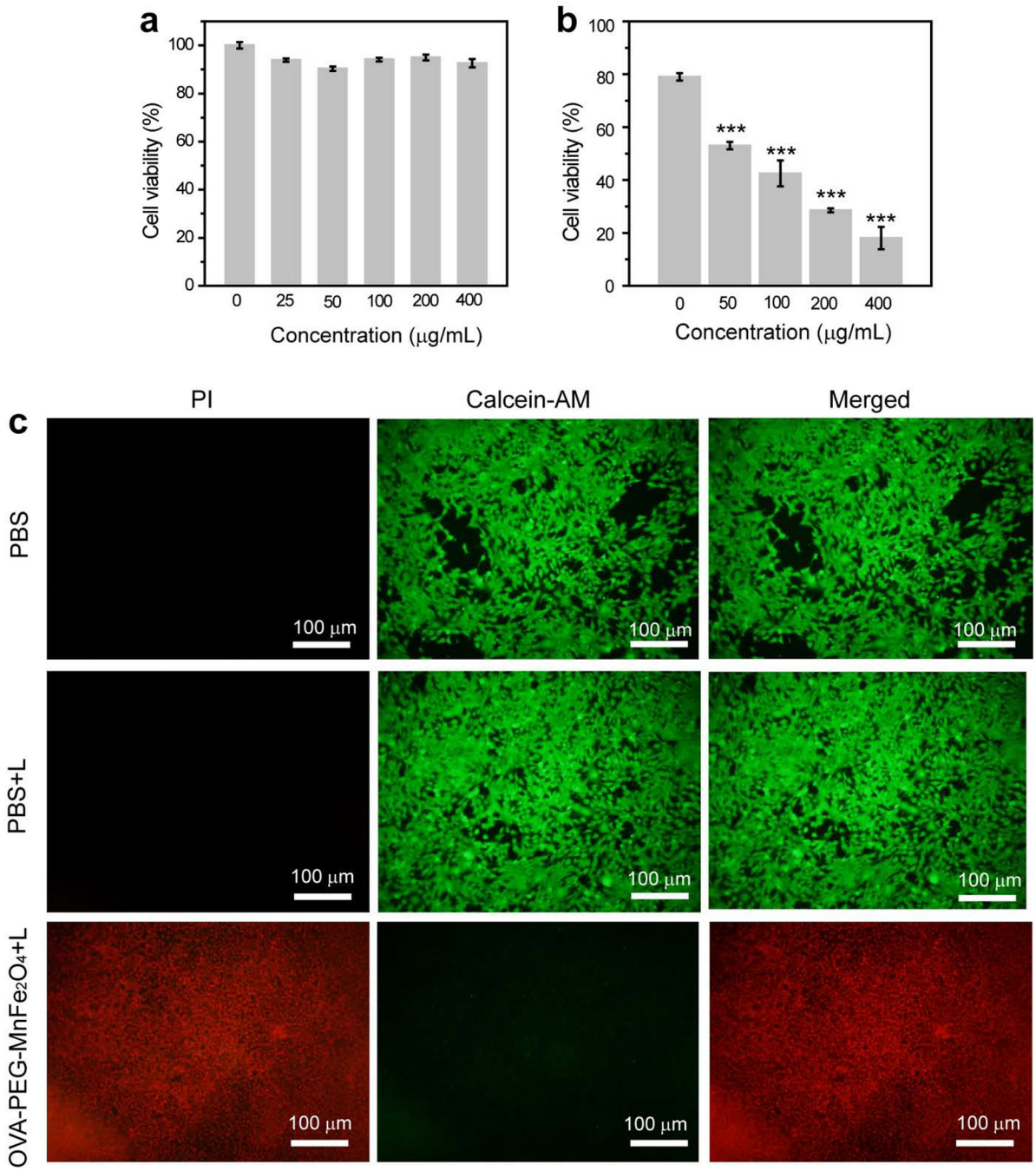

Fig. 2.

Cell viability of 4T1 cells treated by OVA-PEG-$MnFe_2O_4$NPs at different concentrations without (a) or with laser irradiation (b, ***$p < 0.001$, vs. PBS control). (c) Fluorescence images of cells treated with PBS, PBS plus laser irradiation, or OVA-PEG-$MnFe_2O_4$NPs ([$MnFe_2O_4$] = 400 μg/mL) plus laser irradiation (green fluorescence related to live cells, and red fluorescence related to dead cells).

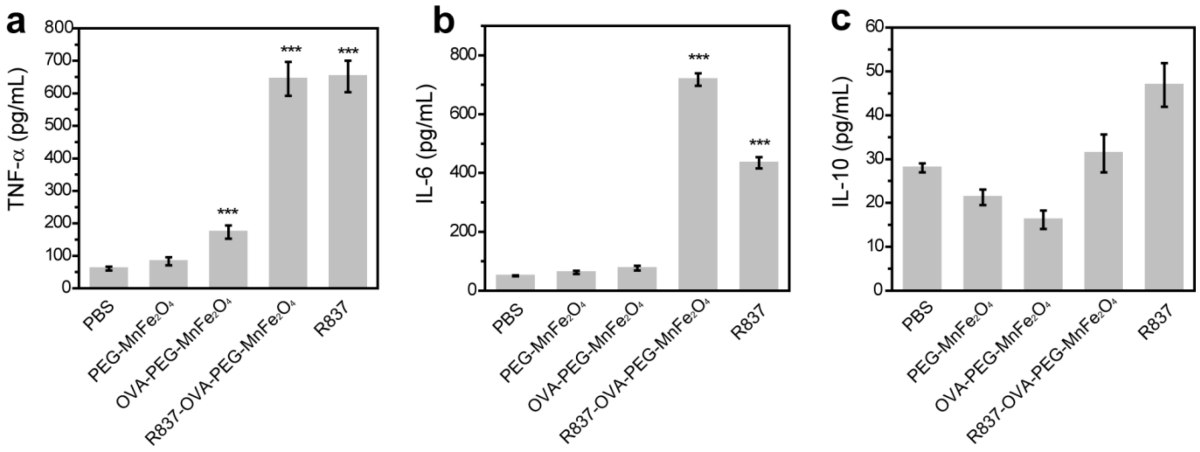

Fig. 3.

The cytokines including TNF-α (a), IL-6 (b), and IL-10 (c) of DC2.4 cells after different treatments for 24 h (n = 3, ***$p < 0.001$, vs. PBS control).

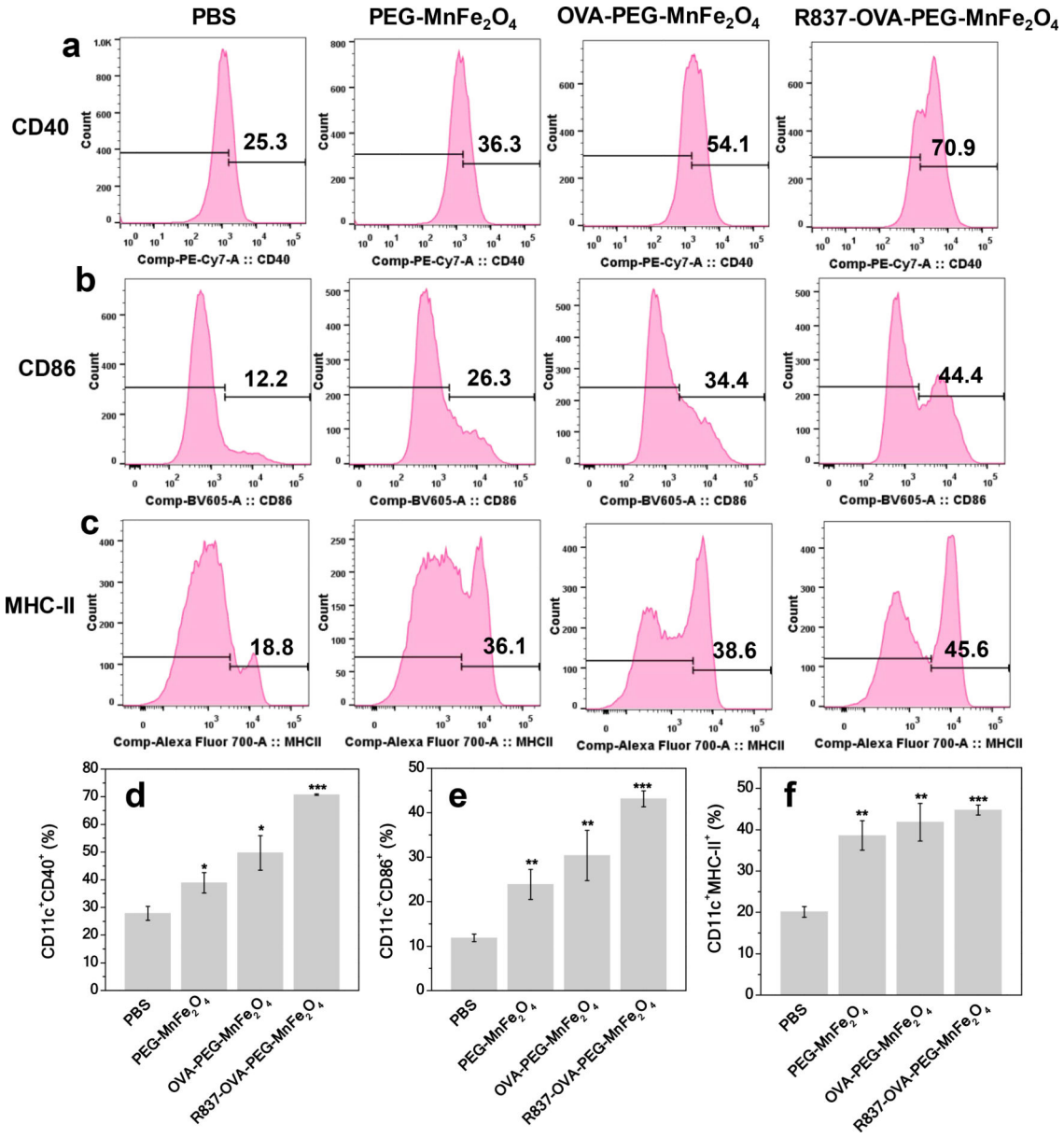

Fig. 4.

Quantification of CD40 (a, d), CD86 (b, e), and MHC-II (c, f) expression in BMDCs after different treatments for 24 h, followed by flow cytometry analysis (n = 3, $^{**}p < 0.01$, $^{***}p < 0.001$, vs. PBS control).

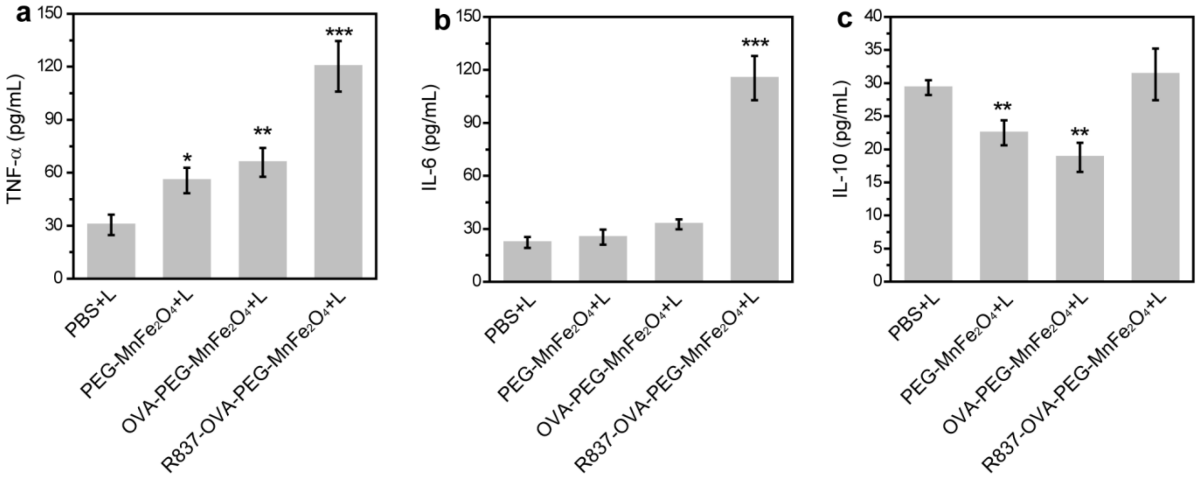

Fig. 5.

Cytokine levels of TNF-α (a), IL-6 (b), and IL-10 (c) in serum from mice isolated on day 3 after different treatments (n = 3, $*P < 0.05$, $**P < 0.01$, $***P < 0.001$, vs. PBS plus laser irradiation group).

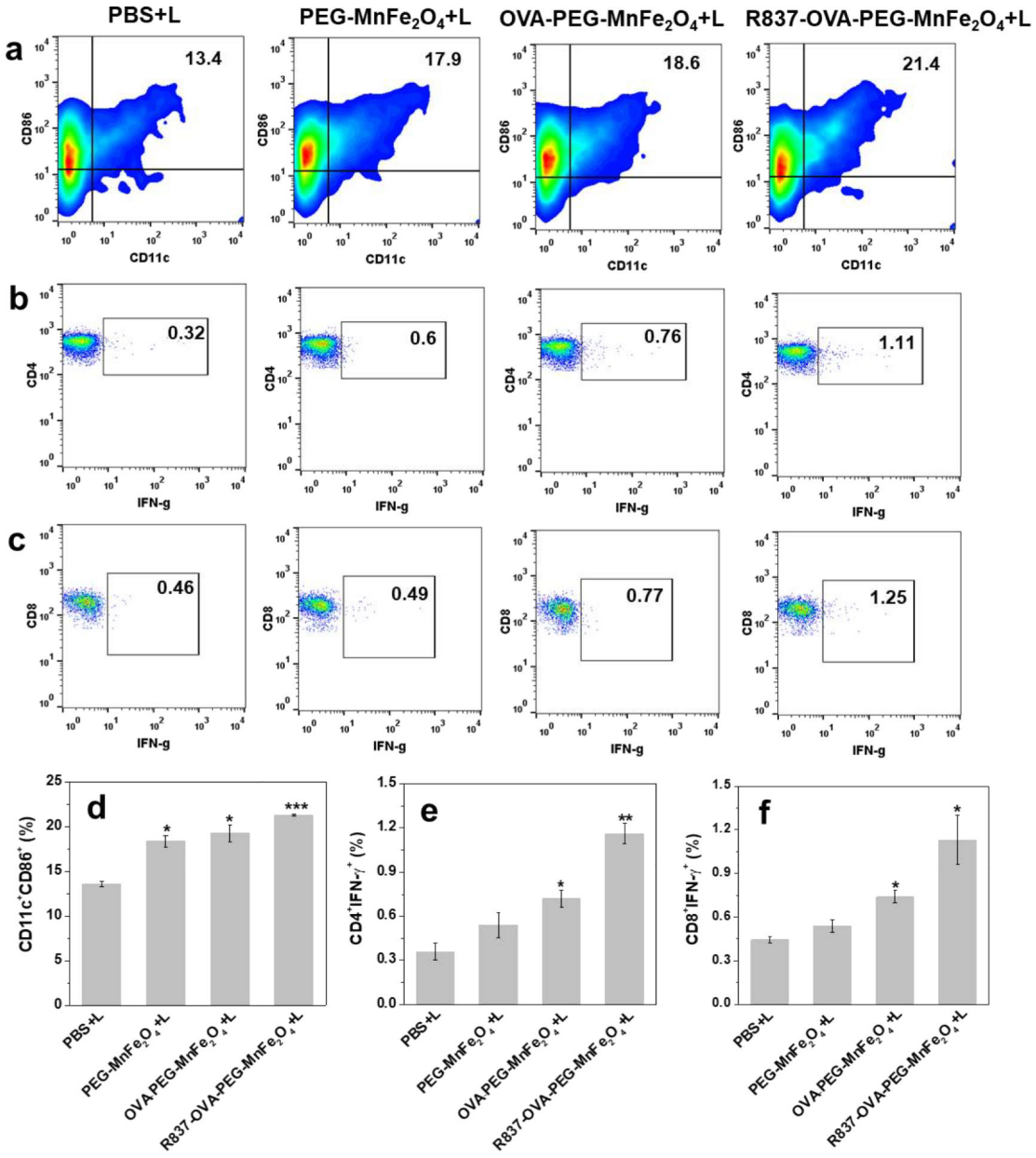

Fig.6.

(a, d) Maturation of DCs in lymph nodes (%) on day 3 after different treatments. (b, e) Representative flow plots used to evaluate frequency of IFN-γ producing CD4 T cells taken from splenocytes of animals on day 7 after various treatments. (c, f) Representative flow plots used to evaluate frequency of IFN-γ producing CD8 T cells taken from splenocytes of animals on day 7 after various treatments (n = 3, $*P < 0.05$, $**P < 0.01$, vs. PBS plus laser irradiation group).

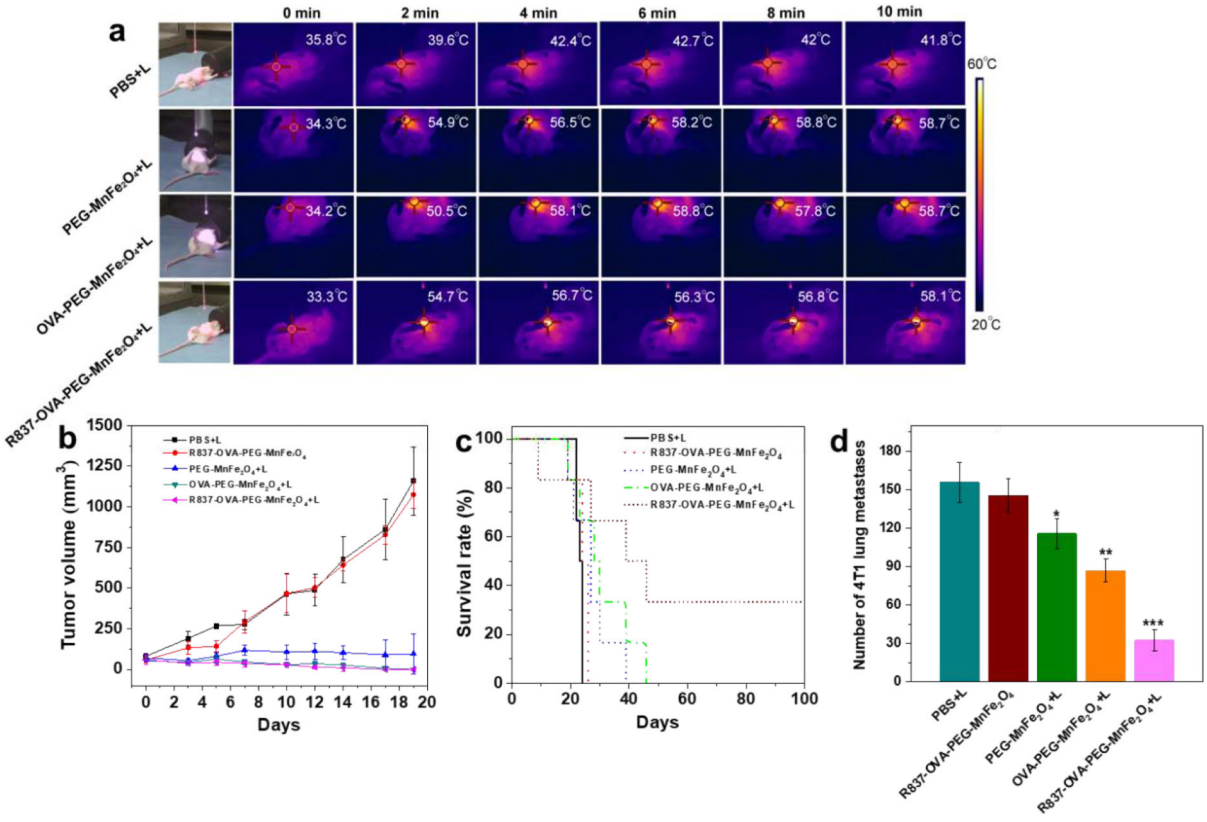

Fig. 7.

(a) Infrared thermal images of the orthotopic 4T1 breast tumor-bearing mice after different treatments through intratumoral injection. Tumor volumes (b) and survival rates (c) of orthotopic 4T1 breast tumor-bearing mice after various treatments. (d) Number of 4T1 lung metastases 15 days after various treatments (n = 3, $*P < 0.05$, $**P < 0.01$, $***P < 0.001$, vs. PBS+L control).

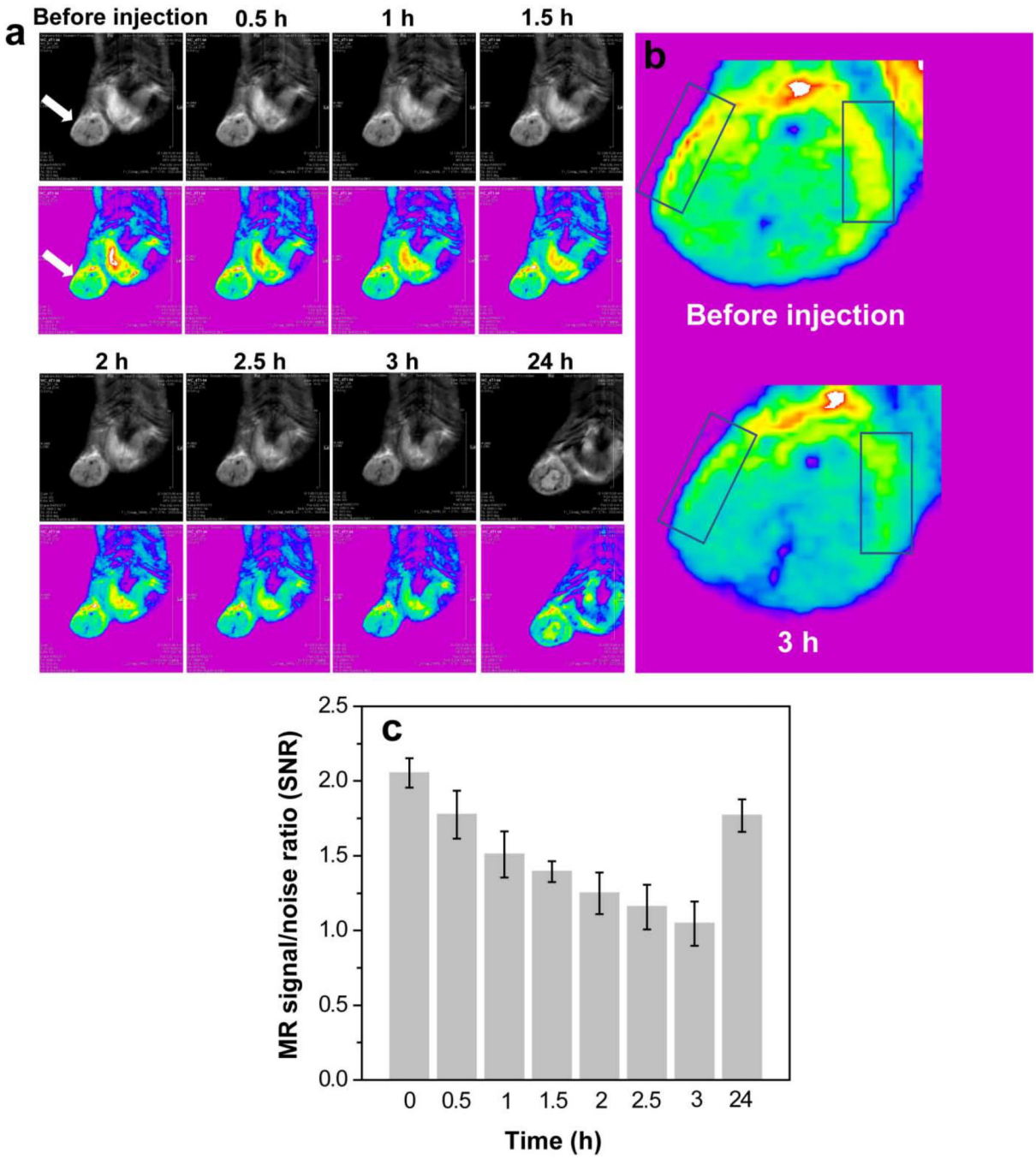

Fig. 8.

T_2-weighted MR images (a) and MR signal/noise ratio (c) of orthotopic 4T1 breast tumor after intravenous injection of PEGylated $MnFe_2O_4$ NPs (white arrows refer to tumor regions). (b) Tumor enlarged MR images at before injection and 3 h postinjection (boxes refer tumor edges).

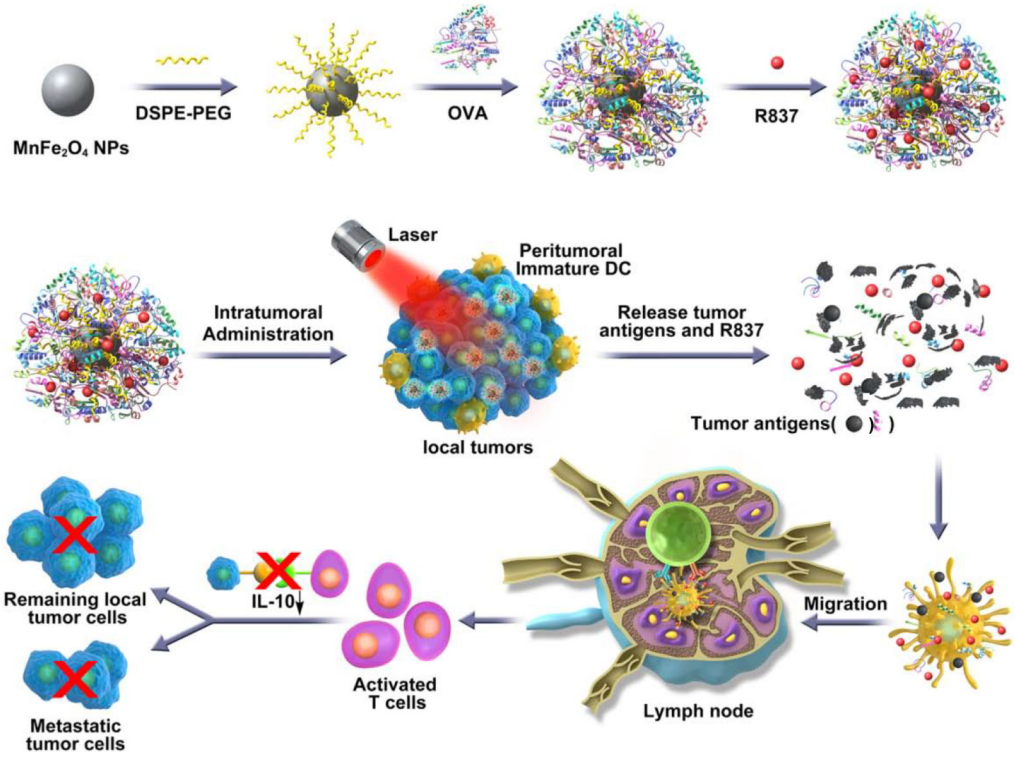

Scheme 1.

Schematic illustration of the synthesis of R837-OVA-PEG-$MnFe_2O_4$ NPs and the mechanism of antitumor immune responses trigged by the nanoplatform under laser irradiation.